

Effective N -body models of composite collisionless stellar systems

Carlo Nipoti^{1*}, Giacomo Cherchi¹, Giuliano Iorio^{2,3,4} and Francesco Calura⁵

¹*Department of Physics and Astronomy, University of Bologna, via Gobetti 93/2, I-40129 Bologna, Italy*

²*Physics and Astronomy Department Galileo Galilei, University of Padova, Vicolo dell'Osservatorio 3, I-35122, Padova, Italy*

³*INFN-Padova, Via Marzolo 8, I-35131 Padova, Italy*

⁴*INAF-Padova, Vicolo dell'Osservatorio 5, I-35122 Padova, Italy*

⁵*INAF - Astrophysics and Space Science Observatory of Bologna, via Gobetti 93/3, I-40129, Bologna, Italy*

Accepted 2021 March 10. Received 2021 March 8; in original form 2020 December 11

ABSTRACT

Gas-poor galaxies can be modelled as composite collisionless stellar systems, with a dark matter halo and one or more stellar components, representing different stellar populations. The dynamical evolution of such composite systems is often studied with numerical N -body simulations, whose initial conditions typically require realizations with particles of stationary galaxy models. We present a novel method to conceive these N -body realizations, which allows one to exploit at best a collisionless N -body simulation that follows their evolution. The method is based on the use of an effective N -body model of a composite system, which is in fact realized as a one-component system of particles that is interpreted *a posteriori* as a multi-component system, by assigning in post-processing fractions of each particle's mass to different components. Examples of astrophysical applications are N -body simulations that aim to reproduce the observed properties of interacting galaxies, satellite galaxies and stellar streams. As a case study we apply our method to an N -body simulation of tidal stripping of a two-component (dark matter and stars) satellite dwarf galaxy orbiting in the gravitational potential of the Milky Way.

Key words: dark matter – galaxies: evolution – galaxies: interactions – galaxies: kinematics and dynamics – methods: numerical

1 INTRODUCTION

Collisionless N -body simulations are standard tools to study the evolution of stellar systems such as galaxies and clusters of galaxies, with typical applications ranging from stability analysis, to the study of galaxy interactions and mergers, tidal stripping of satellites, and dynamical friction. When the phenomenon studied with the N -body simulation involves composite collisionless stellar systems, to set up the initial conditions it is often necessary to build N -body realizations of stationary multi-component models. Here we present effective N -body models that allow one to study efficiently the evolution of such composite systems.

The approach presented here can be used in several studies of galactic dynamics, provided the studied galaxies are gas-poor, so that they can be modelled as multi-component stellar systems, with dark matter (DM) halos and one or more stellar components, representing different stellar populations. Examples of potential applications are N -body simulations of tidal stripping aimed at reproducing the observed properties of satellite dwarf galaxies (e.g. Battaglia et al. 2015; Ural et al. 2015; Sanders et al. 2018; Iorio et al. 2019) or those of tidal streams (e.g. Łokas et al. 2010; Dierickx & Loeb 2017; Laporte et al. 2018; Vasiliev et al. 2020) in the Milky Way. But, more generally, the effective N -body models presented here can be used in N -body simulations of dissipationless galaxy mergers (e.g. Nipoti et al. 2003a; Boylan-Kolchin et al.

2006; Frigo & Balcels 2017) or of the dynamical evolution of galaxies in clusters of galaxies (e.g. Nipoti et al. 2003b; Laporte et al. 2013).

The method proposed in this paper builds on and bears resemblance with other techniques previously proposed in the literature. The key of the effective N -body models considered here is to design composite stellar system starting from the total distribution function (DF) and then obtain its component by subtraction. In the literature, there are a few other studies in which composite stellar systems are built starting from the total DF or mass density distribution. Evans (1993, 1994) built axisymmetric composite stellar systems with total logarithmic or power-law gravitational potential, starting from the analytic DF of the total distribution. Other authors (Hiotelis 1994; Ciotti et al. 2009; Ciotti & Ziaee Lorzad 2018; Ciotti et al. 2019) used instead the total mass density distribution as starting point to build multi-component anisotropic spherical stellar systems. White (1980) and Ciotti et al. (1995) used a technique similar to the one used in this work to build equilibrium models of isotropic or radially anisotropic spherical stellar systems with metallicity gradients (see also Nipoti et al. 2003b and Nipoti et al. 2020). Within this framework, here for the first time we exploit the idea of building different components by subtraction from the total DF to envisage a very effective and general method for N -body modelling. This method allows us to use N -body simulations involving only one-component systems to model the dynamical evolution of entire families of composite stellar systems, with stars and DM.

The paper is organized as follows. In Section 2 we review the

* E-mail: carlo.nipoti@unibo.it

properties of stationary composite collisionless stellar systems and introduce the concept of their effective N -body modelling. In Section 3 we extend our view to the dynamical evolution of such systems, when they are not isolated. Section 4 treats in more detail the case of two-component spherical isotropic systems. In Section 5 we present the application of our method to an N -body simulation of tidal stripping. Section 6 concludes.

2 STATIONARY COMPOSITE COLLISIONLESS STELLAR SYSTEMS

2.1 Distribution functions and portion functions

Let us consider a stationary composite stellar system with N_{comp} components, in which the k -th component has DF f_k . The total DF is $f_{\text{tot}} = \sum_{k=1}^{N_{\text{comp}}} f_k$. The total gravitational potential Φ_{tot} generated by these components satisfies the Poisson equation

$$\nabla^2 \Phi_{\text{tot}}(\mathbf{x}) = 4\pi G \rho_{\text{tot}}(\mathbf{x}), \quad (1)$$

where

$$\rho_{\text{tot}}(\mathbf{x}) = \int f_{\text{tot}} d^3 \mathbf{v} \quad (2)$$

is the total mass density distribution, and \mathbf{x} and \mathbf{v} are, respectively, the position and velocity vectors. We know from Jeans' theorem (e.g. Binney & Tremaine 2008) that the DFs of stationary collisionless stellar systems depend on the phase-space coordinates (\mathbf{x}, \mathbf{v}) through $n \leq 3$ integrals of motion $\mathbf{I} = I_1, \dots, I_n$, which are functions of (\mathbf{x}, \mathbf{v}) that are conserved along the orbits. If we extract from $f_{\text{tot}} = f_{\text{tot}}(\mathbf{I})$ an orbit with integrals of motion \mathbf{I} , the probability that a particle on such orbit belongs to the k -th component is

$$\mathcal{P}_k(\mathbf{I}) = \frac{f_k(\mathbf{I})}{f_{\text{tot}}(\mathbf{I})}. \quad (3)$$

In this paper we will refer to the function $\mathcal{P}_k(\mathbf{I})$ as the *portion function* of the k -th component.

2.2 N -body realizations

2.2.1 Standard multi-component N -body model

The standard approach to build an N -body realization of a stationary multi-component stellar system is to represent the k -th component with N_k particles with phase-space coordinates extracted from the DF $f_k(\mathbf{I})$, with $\mathbf{I} = \mathbf{I}(\mathbf{x}, \mathbf{v})$: the j -th particle ($j = 1, \dots, N_k$) has mass m_j , phase-space coordinates $(\mathbf{x}_j, \mathbf{v}_j)$ and integrals of motion $\mathbf{I}_j = \mathbf{I}(\mathbf{x}_j, \mathbf{v}_j)$. The total number of particles is $N_{\text{tot}} = \sum_k N_k$. Jeans' theorem guarantees that each component of this N -body realization is stationary, because its particles are extracted from a DF depending only on integrals of motions. In this approach, in the N -body realization we assign to each particle a given “kind”, for instance “DM particle” or “stellar particle” if it belongs to, respectively, the DM halo or the stellar component. In a purely collisionless N -body system the orbits of particles are determined only by gravity and are thus independent of the particle kind and on the particle mass. This suggests to explore different N -body realizations in which the particles are not labelled as being of a given kind or belonging to a given component. In the following we introduce such an alternative approach.

2.2.2 Effective multi-component N -body model

Instead of extracting a set of particles for each component, as in the standard method described above, we can construct an N -body realization of a stationary composite stellar system by extracting N_{tot} particles from the total DF $f_{\text{tot}}(\mathbf{I})$, obtaining for the i -th particle a set of phase-space coordinates $(\mathbf{x}_i, \mathbf{v}_i)$ and corresponding integrals of motion $\mathbf{I}_i = \mathbf{I}(\mathbf{x}_i, \mathbf{v}_i)$ ($i = 1, \dots, N_{\text{tot}}$). In this way, we do not assign a given particle to one of the components, but we can nevertheless interpret our system as multi-component as follows. Given that $\mathcal{P}_k(\mathbf{I}_i)$ is the probability that the i -th particle belongs to the k -th component (equation 3), the mass contribution of the i -th particle to the k -th component is $\xi_{k,i} m_i$, where m_i is the mass of the i -th particle and $\xi_{k,i} \equiv \mathcal{P}_k(\mathbf{I}_i)$ is the mass fraction of the i -th particle that belongs to the k -th component. For instance in a two-component system with a stellar component (with DF f_{\star}) and DM component (with DF $f_{\text{DM}} \equiv f_{\text{tot}} - f_{\star}$), the i -th particle has stellar mass $\xi_{\star,i} m_i$ and DM mass $\xi_{\text{DM},i} m_i$, where $\xi_{\star,i} = \mathcal{P}_{\star}(\mathbf{I}_i)$ and $\xi_{\text{DM},i} = 1 - \xi_{\star,i}$ are, respectively, its stellar and DM mass fractions, and $\mathcal{P}_{\star}(\mathbf{I}) \equiv f_{\star}(\mathbf{I})/f_{\text{tot}}(\mathbf{I})$ is the portion function (equation 3) of the stellar component. For any choice of $\mathcal{P}_k(\mathbf{I})$ the k -th component is univocally defined. For instance, the total mass of the k -th component is $M_k = \sum_i \xi_{k,i} m_i$, and similarly one can compute the mass density and velocity distributions of the k -th component simply by weighting the contribution of the i -th particle by $\xi_{k,i} m_i$. If such an N -body system is evolved in isolation, the properties (e.g. density and velocity distributions) of all its N_{comp} components are time-independent in the limit¹ $N_{\text{tot}} \rightarrow \infty$, because $f_{\text{tot}}(\mathbf{I})$ is the DF of a stationary system and $\mathcal{P}_k(\mathbf{I})$ is a function of the integrals of motions. The main advantage of this method with respect to the standard method (Section 2.2.1) is that $\mathcal{P}_k(\mathbf{I})$ must not be specified *a priori*, so each simulation can be interpreted in infinite different ways by assuming $\mathcal{P}_k(\mathbf{I})$ *a posteriori*. Of course, the aim of N -body simulations is to study systems whose physical properties evolve in time: in the next section we move to discuss such a case.

3 DYNAMICAL EVOLUTION OF COMPOSITE COLLISIONLESS STELLAR SYSTEMS

N -body simulations are often used to study the dynamical evolution, in the presence of an external perturbation, of stellar systems that are initially close to equilibrium. Examples are simulations of the evolution of satellite stellar systems orbiting within a host stellar system (for instance satellite galaxies orbiting within a host galaxy) or simulations of galaxy mergers. In order to illustrate our approach, let us focus on the case of satellites and consider, for instance, the simulation of a satellite dwarf galaxy made of stars and DM orbiting in a host galaxy. As often done in this kind of simulations, we assume that the host galaxy is represented simply as a static gravitational potential, while the satellite is represented with particles as a two-component N -body system (with a stellar component and a DM halo) that would be in equilibrium if isolated (e.g. Battaglia et al. 2015).

3.1 Standard multi-component N -body models

In the standard method the satellite is set up as a two-component stationary stellar system with N_{\star} stellar particles extracted from a DF f_{\star} and N_{DM} DM particles extracted from a DF f_{DM} , both

¹ Of course this is not true, strictly speaking, for finite N_{tot} because of discreteness effects.

in equilibrium in the total gravitational potential of the satellite $\Phi_{\text{tot}} = \Phi_{\star} + \Phi_{\text{DM}}$. The total density distribution of the satellite is $\rho_{\text{tot}} = \rho_{\star} + \rho_{\text{DM}}$, where ρ_{\star} is the density of the stellar component and ρ_{DM} is the density of the DM component. At the initial time of the simulation the phase-space coordinates of the centre of mass of the satellite are assigned so that the satellite is in orbit in the fixed external gravitational potential of the host galaxy. Due to the tidal interaction with the gravitational field of the host galaxy, the satellite evolves modifying the distributions of its components, for instance producing tidal tails, and losing stellar and DM particles via tidal stripping. The relative distribution of the dark and stellar components of the satellite are fixed in the initial conditions, so the outcome of the simulation is univocal. To explore the evolution of a satellite on the same orbit, with the same total distribution function $f_{\text{tot}} = f_{\star} + f_{\text{DM}}$, but with different dark and stellar DFs, a new *N*-body simulation is necessary in this standard approach.

3.2 Effective multi-component *N*-body models

When the effective multi-component *N*-body modelling is used, the satellite is set up as a one-component stellar system with N_{tot} particles extracted from a DF $f_{\text{tot}}(\mathbf{I})$, with total density distribution ρ_{tot} . As in the standard approach (Section 3.1), at the initial time of the simulation the satellite is put in orbit in the fixed external gravitational potential of the host galaxy, and the evolution of all the particles is followed for the time spanned by the simulation. The simulation is then interpreted, *a posteriori*, by assigning to each particle a stellar mass and a DM mass, by choosing a stellar portion function $\mathcal{P}_{\star}(\mathbf{I})$, where \mathbf{I} are the integrals of motion of the particle *when the satellite is set up in equilibrium and isolated*. In practice, if the *i*-th particle has mass m_i , its stellar mass is $m_{\star,i} = \mathcal{P}_{\star}(\mathbf{I}_i)m_i$ and its DM mass is $m_{\text{DM},i} = m_i - m_{\star,i} = [1 - \mathcal{P}_{\star}(\mathbf{I}_i)]m_i$, where \mathbf{I}_i are the values of the integrals of motion of the *i*-th particle in the isolated satellite. For given \mathcal{P}_{\star} , from the simulation we can infer the evolution of the stellar and DM components of the satellite, separately, for instance measuring the stellar and DM mass loss due to tidal stripping. The same simulation can be reinterpreted in infinite ways by choosing different \mathcal{P}_{\star} .

4 A SIMPLE CASE: TWO-COMPONENT ISOTROPIC SPHERICAL SYSTEMS

Here we present an application of the effective *N*-body models introduced above to spherical two-component collisionless stellar systems with isotropic velocity distributions.

4.1 Two-component spherical stellar systems with ergodic distribution functions

The simplest family of multi-component collisionless stellar systems generated by DFs is the family of two-component spherical stellar systems with isotropic velocity distribution. In this case the DFs of both components are ergodic, i.e. they are functions only of the energy per unit mass E . For the sake of clarity, we specialize to the case in which one of the component is the stellar component, with DF $f_{\star}(\mathcal{E})$, and the other is the DM halo, with DF $f_{\text{DM}}(\mathcal{E})$, where $\mathcal{E} = -E$ is the relative energy per unit mass. The total distribution function is $f_{\text{tot}}(\mathcal{E}) = f_{\star}(\mathcal{E}) + f_{\text{DM}}(\mathcal{E})$. As explained in Sections 2.2.2 and 3.2, when building an effective *N*-body model of such a system, we consider a single component with DF $f_{\text{tot}}(\mathcal{E})$. The stellar and DM components are defined by choosing a stellar portion function

$0 \leq \mathcal{P}_{\star}(\mathcal{E}) \leq 1$, so $0 \leq f_{\star}(\mathcal{E}) \leq f_{\text{tot}}(\mathcal{E}) \forall \mathcal{E}$. The portion function of the DM component is $\mathcal{P}_{\text{DM}}(\mathcal{E}) = 1 - \mathcal{P}_{\star}(\mathcal{E})$, so $0 \leq f_{\text{DM}}(\mathcal{E}) \leq f_{\text{tot}}(\mathcal{E}) \forall \mathcal{E}$. One-component systems with the same $f_{\text{tot}}(\mathcal{E})$ can be interpreted as different two-component systems, depending on the choice of $\mathcal{P}_{\star}(\mathcal{E})$. For instance, for an isolated spherical isotropic system with DF $f_{\text{tot}}(\mathcal{E})$, the stellar density profile is

$$\rho_{\star}(r) = 4\pi \int \mathcal{P}_{\star}(\mathcal{E}) f_{\text{tot}}(\mathcal{E}) v^2 dv, \quad (4)$$

where $\mathcal{E}(r, v) = \Psi_{\text{tot}}(r) - \frac{1}{2}v^2$ and $\Psi_{\text{tot}}(r) = -\Phi_{\text{tot}}(r)$ is the relative total potential (here r is the spherical radial coordinate and v the magnitude of the velocity vector). The DM density distribution is

$$\rho_{\text{DM}}(r) = 4\pi \int [1 - \mathcal{P}_{\star}(\mathcal{E})] f_{\text{tot}}(\mathcal{E}) v^2 dv. \quad (5)$$

4.2 An analytic expression of the portion function

Our aim is to have an analytic expression of $\mathcal{P}_{\star}(\mathcal{E})$, depending on a handful of parameters, flexible enough to represent realistic stellar components of spheroids. In this work we adopt as analytic expression of the portion function for spherical isotropic systems the four-parameter function

$$\mathcal{P}_{\star}(\mathcal{E}) = A \left(\frac{\mathcal{E}}{\mathcal{E}_0} \right)^{\alpha} \exp \left[- \left(\frac{\mathcal{E}}{\mathcal{E}_0} \right)^{\beta} \right], \quad (6)$$

where α, β and A are dimensionless parameters, and \mathcal{E}_0 is a characteristic relative energy. In the following we will refer to this analytic function as generalized Schechter function, because when $\beta = 1$ it reduces to the well known Schechter (1976) function, widely used in a different context to model the galaxy luminosity function. In Section 4.3 we show a representative case in which the generalized Schechter $\mathcal{P}_{\star}(\mathcal{E})$ performs well in producing stellar components with realistic density profiles. However, we stress that the method proposed in this paper can be applied with $\mathcal{P}_{\star}(\mathcal{E})$ with functional forms different from equation (6), for instance with more free parameters if an even more flexible function is required.

4.3 A case study: a system with total Hernquist density profile

Let us focus on the case of a self-gravitating system in which the total density distribution follows a Hernquist (1990) profile:

$$\rho_{\text{tot}}(r) = \frac{M_{\text{tot}}}{2\pi a^3} \frac{1}{(r/a)[1 + (r/a)]^3}, \quad (7)$$

where a is the scale radius and M_{tot} the total mass. This total density distribution is shown in the bottom row of panels of Fig. 1 as a solid curve. The total gravitational potential of the system, related to ρ_{tot} by equation (1), is

$$\Phi_{\text{tot}}(r) = - \frac{GM_{\text{tot}}}{r + a}. \quad (8)$$

The ergodic DF $f_{\text{tot}}(\mathcal{E})$ generating a self-gravitating system with mass density distribution (7) is known analytically (Hernquist 1990) and is shown in the middle row of panels of Fig. 1 as a solid curve.

Such a spherical system with Hernquist total density profile can be split in a stellar component and a DM component by assuming a stellar portion function $\mathcal{P}_{\star}(\mathcal{E})$. In particular, adopting as \mathcal{P}_{\star} the generalized Schechter function (equation 6), we can build stellar components with double power law density profile, whose detailed properties depend on the values of the parameters α, β, A and $\tilde{\mathcal{E}}_0 \equiv \mathcal{E}_0/(GM_{\text{tot}}a^{-1})$. For instance, for $\alpha = 2, \beta = 4, A = 0.3$ and $\tilde{\mathcal{E}}_0 = 0.7$ we obtain the stellar portion function, DF and mass density

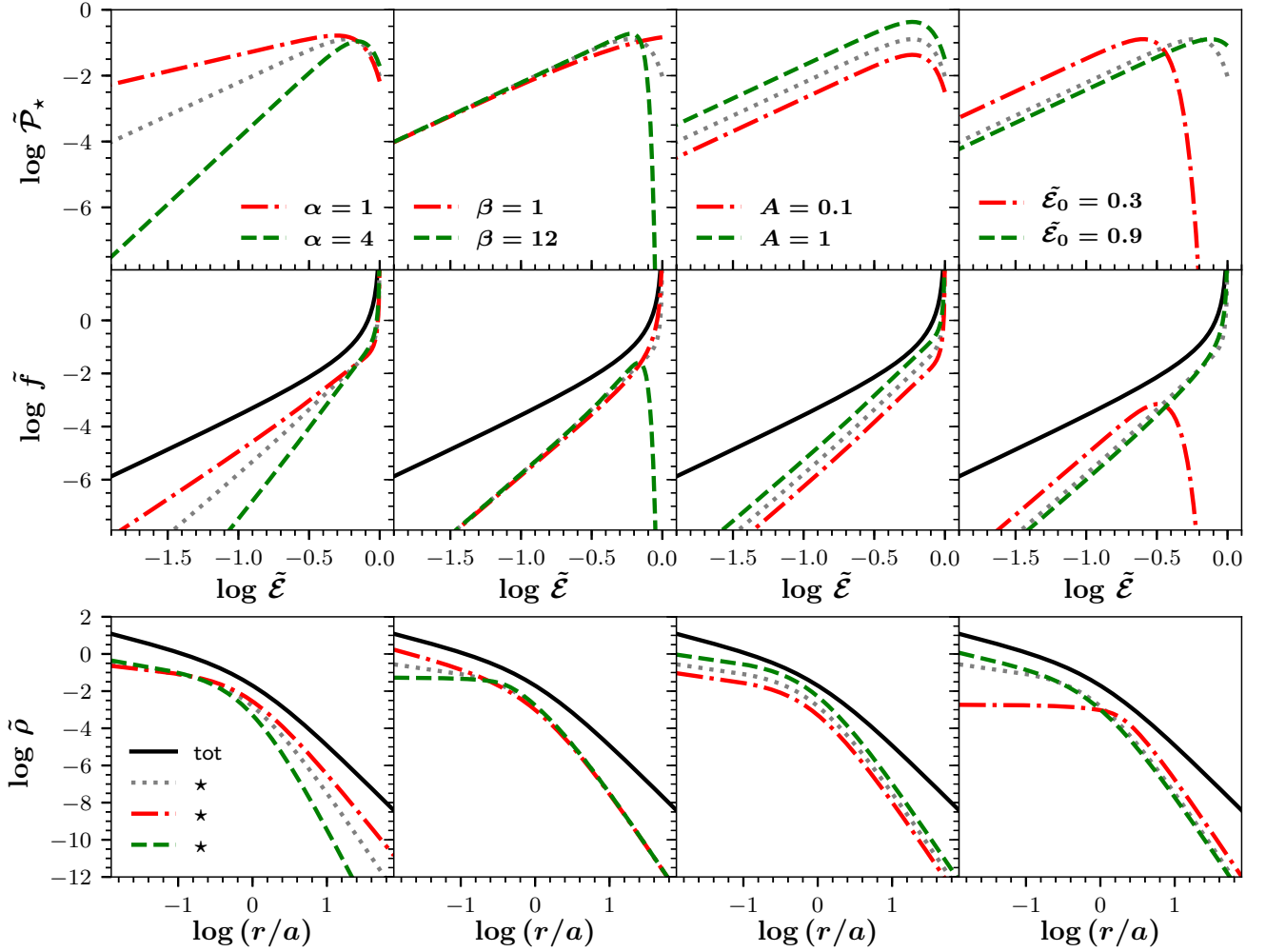


Figure 1. Density $\tilde{\rho} \equiv \rho/(M_{\text{tot}}a^{-3})$ (bottom row of panels) as a function of radius and DF $\tilde{f} \equiv f/(G^3 M_{\text{tot}} a^3)^{-1/2}$ (middle row of panels) as a function of specific relative energy $\tilde{\mathcal{E}} \equiv \mathcal{E}/(GM_{\text{tot}}a^{-1})$ for models with the same total distribution (solid curves), but stellar distributions (dotted, dashed and dot-dashed curves) obtained with different generalized Schechter stellar portion functions \mathcal{P}_* (top row of panels). When not specified otherwise, the parameters of the portion function (equation 6) are $\alpha = 2, \beta = 4, A = 0.3$ and $\tilde{\mathcal{E}}_0 \equiv \mathcal{E}_0/(GM_{\text{tot}}a^{-1}) = 0.7$, which are the values adopted for the model represented by the dotted curves. In each column, the values of the parameters reported in the top panel apply also to the middle and bottom panels. M_{tot} and a are, respectively, the total mass and scale radius of the total density profile, which is a Hernquist sphere (equation 7).

distribution represented by the dotted curves in Fig. 1: the bottom row of panels shows that the resulting density profile is a double power law with logarithmic slope $\gamma_* \equiv d \ln \rho_*/d \ln r \approx -0.5$ in the centre and $\gamma_* \approx -5.5$ in the outskirts. Different slopes can be obtained by changing the values of the parameters. The parameter α determines the probability of having weakly bound stars (i.e. with low relative energy \mathcal{E}): in particular the lower α the shallower the outer stellar density profile (see the leftmost column of panels in Fig. 1). The parameter β determines the probability of having strongly bound stars (i.e. with high \mathcal{E}), in the sense that large values of β penalize the most bound orbits, thus the higher β the shallower the inner stellar density profile (see the second column of panels in Fig. 1): in this case a core of constant density is obtained for $\beta = 12$, while for $\beta = 1$ $\rho_* \propto r^{-1}$ in the centre. The parameter A , which is the normalization of \mathcal{P}_* , does not affect the shape of the stellar density profile but, by shifting vertically $f_*(\mathcal{E})$, it determines the fractional mass contribution of the stellar component, in the sense that the stars contribute more for higher values of A (see the third column of panels in Fig. 1). Finally, the parameter \mathcal{E}_0 tunes the energy $\mathcal{E}_{\text{peak}}$ at which \mathcal{P}_* peaks,

which for the generalized Schechter function is $\mathcal{E}_{\text{peak}} = \mathcal{E}_0 (\alpha/\beta)^{1/\beta}$. Thus, the value of \mathcal{E}_0 influences mainly the position of the knee of the stellar density distribution, which is at larger radii for lower \mathcal{E}_0 (see the rightmost column of panels in Fig. 1). Note, however, that also the logarithmic slope γ_* at radii smaller than the position of the knee changes with \mathcal{E}_0 , because the stellar DF f_* (shown in the second row of panels in Fig. 1) depends not only on \mathcal{P}_* , but also on the shape of f_{tot} . The portion function, DF, and density profile of the DM component, not shown in Fig. 1, can be obtained simply by subtraction: $\mathcal{P}_{\text{DM}} = 1 - \mathcal{P}_*$, $f_{\text{DM}} = f_{\text{tot}} - f_*$ and $\rho_{\text{DM}} = \rho_{\text{tot}} - \rho_*$. All these quantities are guaranteed to be everywhere positive because $\mathcal{P}_* < 1 \forall \mathcal{E}$.

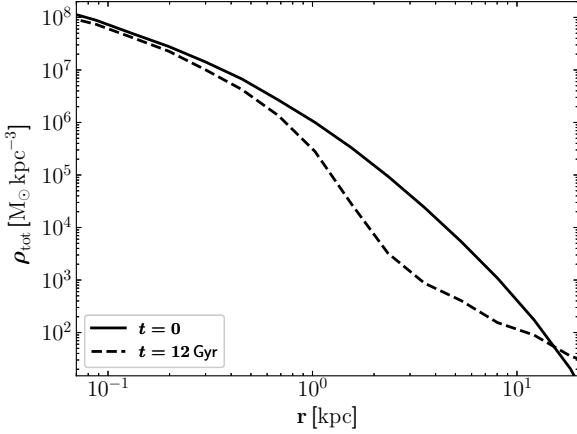


Figure 2. Angle-averaged initial ($t = 0$, solid curve) and final ($t = 12$ Gyr, dashed curve) total (DM plus stars) density profiles of the satellite in the N -body simulation.

5 APPLICATION TO AN N -BODY SIMULATION OF TIDAL STRIPPING

Here, we apply the effective multi-component method described above to an N -body simulation that follows the evolution of a satellite galaxy in the gravitational potential of the Milky Way.

5.1 Set-up of the N -body simulation

The initial conditions of the N -body realization of the satellite have been produced using the Python module `OpOpGadget`² developed by G. Iorio. The N -body system is realized as a one-component spherical isotropic stellar system with density profile

$$\rho_{\text{tot}}(r) = \frac{\rho_0}{(r/a)[1 + (r/a)]^3} \exp\left[-\left(\frac{r}{r_t}\right)^2\right], \quad (9)$$

representing the total (DM plus stellar) distribution of the satellite, which is a Hernquist profile (equation 7) exponentially truncated at r_t . In particular, we adopt $a = 0.9$ kpc, $r_t = 17$ kpc and central density ρ_0 such that the total mass of the system is $M_{\text{tot}} \equiv 4\pi \int_0^\infty \rho_{\text{tot}}(r)r^2 dr = 4.5 \times 10^7 M_\odot$. The satellite's initial total density distribution in physical units is shown in Fig. 2 as a black solid line. The number of particles is $N_{\text{tot}} = 10^5$, and all particles have the same mass $m = M_{\text{tot}}/N_{\text{tot}} = 450 M_\odot$. The positions and velocities of the N_{tot} particles are assigned in Cartesian coordinates (relative to the satellite's centre of mass) as in Iorio et al. (2019), using the ergodic DF $f_{\text{tot}}(\mathcal{E})$ obtained numerically via Eddington's inversion formula (Eddington 1916). The N -body system is in equilibrium if isolated, as we verified by running a simulation with the same initial conditions as that presented in this work, but with the satellite in isolation, i.e. without the Milky Way external potential.

The simulation was run using the collisionless code `FVFP` (Londrillo et al. 2003; Nipoti et al. 2003a) with the addition of the axisymmetric Milky Way model of Johnston et al. (1995) as external static gravitational potential (see Battaglia et al. 2015). We adopted $\theta_{\text{min}} = 0.5$ as the minimum value of the opening parameter, softening length $\epsilon = 0.02$ kpc and constant time step $\Delta t = 0.01 t_{\text{dyn}}$, where $t_{\text{dyn}} = 1/\sqrt{G\bar{\rho}_h}$ is the initial dynamical time of the satellite and $\bar{\rho}_h$ is

its initial average density within the stellar half-mass radius r_h . For the adopted initial conditions $t_{\text{dyn}} \approx 3.5 \times 10^8$ yr.

As orbit of the satellite we assume the orbit dubbed P07ecc in Battaglia et al. (2015), which is almost polar with eccentricity ≈ 0.4 and pericentric radius ≈ 61 kpc. At the initial time of the simulation the phase-space coordinates of the centre of mass of the satellite are $(x, y, z) = (35.814, 0, 137.389)$ kpc and $(v_x, v_y, v_z) = (-94.875, -77.81, 2.901)$ km s⁻¹, in a Cartesian coordinate system, centred in the Galactic centre, in which xy is the Galactic equatorial plane. The simulation is evolved for 12 Gyr. For each snapshot of the simulation we measure the angle-averaged density distribution $\rho_{\text{tot}}(r)$ and integrated total mass distribution $M(r)$, by binning the particles in concentric spherical shells. Here r is the distance from the satellite's centre, which is defined as the position of the peak of the density distribution of the satellite, computed as in Iorio et al. (2019). In a similar way, for given stellar portion function \mathcal{P}_* , we can measure for each snapshot the angle-averaged stellar density distribution $\rho_*(r)$ and stellar mass profile $M_*(r)$, by weighting the particles' masses as described in Section 2.2.2. The DM density and mass distributions are obtained using as portion function $\mathcal{P}_{\text{DM}} = 1 - \mathcal{P}_*$.

5.2 Results

5.2.1 Evolution of the total mass distribution

The projected total (DM plus stars) density distribution of the satellite at different times in the simulation is shown in Fig. 3 (left column of panels), for a line of sight parallel to the equatorial plane of the Milky Way. As expected, the initially spherical density distribution of the satellite is distorted by the interaction with the tidal force field of the Milky Way, which produces two significant tidal tails, one leading and one trailing, departing from the main body of the disrupting satellite. However, as illustrated by the zoomed-in surface density maps in the insets in Fig. 3, the central regions remain close to spherical symmetry. While the central total density profile hardly evolves, at larger radii the total density profile changes drastically with time, and at $t = 12$ Gyr (black dashed curve in Fig. 2) it is heavily truncated at $r \approx 1$ kpc and characterized by a shallow tail at $r \approx 10$ kpc produced by the stripped particles. To quantify the mass loss we take as reference mass at each time the mass $M_{3\text{kpc}}$ of all the particles within a sphere of radius $r = 3$ kpc from the centre of the satellite. The choice of 3 kpc as reference radius (which is about twice the initial half-mass radius) is somewhat arbitrary, but is empirically motivated by the requirement to include most of the stellar mass at $t = 0$ (see Section 5.2.2) and to exclude most of the stellar tidal tails in the subsequent snapshots (see insets in Fig. 3). We note that $M_{3\text{kpc}} \approx 0.69 M_{\text{tot}}$ at $t = 0$. The black curve in Fig. 4, which plots $M_{3\text{kpc}}$ as a function of time, shows that, within 3 kpc, the satellite loses almost 70% of its initial mass over 12 Gyr of evolution.

5.2.2 Evolution of the stellar and dark matter mass distributions

The simulation is interpreted *a posteriori* in different ways by choosing different portion functions $\mathcal{P}_*(\mathcal{E})$, where \mathcal{E} is the initial particle relative energy, computed for the isolated satellite. Here we consider two models: *model C*, in which the initial stellar distribution is more compact, and *model E*, in which the initial stellar distribution is more extended. Both models are obtained assuming as functional form of \mathcal{P}_* the generalized Schechter function (equation 6). The values of the parameters of \mathcal{P}_* are $\alpha = 3, \beta = 1, A = 1.35$, and $\tilde{\mathcal{E}}_0 = 0.8$ for model C, and $\alpha = 0.5, \beta = 12, A = 0.5$ and $\tilde{\mathcal{E}}_0 = 0.7$ for model E. The initial stellar density profile of model C (red solid curve in

² <https://github.com/iogiul/OpOpGadget>

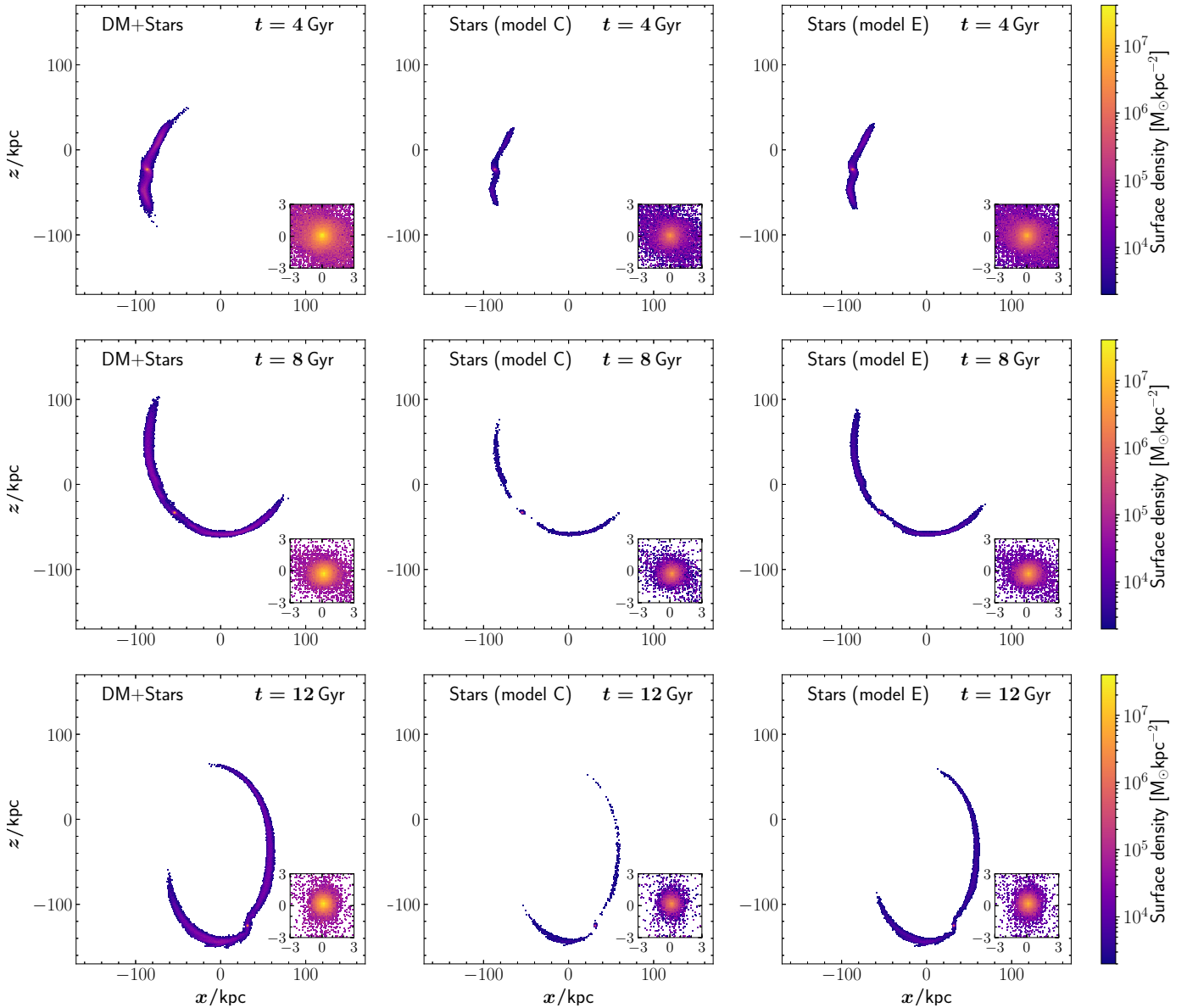


Figure 3. *Left column of panels.* Total (DM plus stars) mass surface density distribution of the satellite in the N -body simulation at $t = 4$ Gyr (top panel), $t = 8$ Gyr (middle panel) and $t = 12$ Gyr (bottom panel), for a line of sight along the y axis, in the adopted Cartesian coordinate system, centred in the Galactic centre, in which the z axis is orthogonal to the Galactic equatorial plane xy . *Middle column of panels.* Same as left column of panels, but showing the stellar mass surface density distribution of the satellite according to model C. *Right column of panels.* Same as middle column of panels, but for model E. In each panel the inset represents a zoomed-in surface density map of $3 \text{ kpc} \times 3 \text{ kpc}$ centred in the peak of the density distribution of the satellite.

upper left panel of Fig. 5) has a central cusp ($\rho_* \propto r^{-1}$) and declines steeply in the outer parts, while the stellar density profile of model E (green solid curve in upper right panel of Fig. 5) has a central core ($\rho_* \propto \text{constant}$) and is shallower in the outskirts. The position of the knee of the stellar density profile (i.e. the radius of transition between inner and outer slope) occurs at larger radius for model E than for model C.

The stellar and DM density and mass profiles at different times in the simulation are shown in Fig. 5 for model C in the left column of panels and for model E in the right column of panels. In model E the initial DM density is higher than the initial stellar density at all radii. In model C the initial stellar density is higher than the DM density in the centre ($r \lesssim 200 \text{ pc}$), while the dark halo dominates at

larger radii. In both cases the evolution of the DM density profile resembles that of the total mass distribution, with substantial losses at large radii. The evolution of the stellar component is instead very different in the two cases: the stellar distribution of model C remains almost unaltered for 12 Gyr, while it is heavily stripped in model E. The fractional stellar mass loss for the two models is quantified in Fig. 4 using as reference the stellar mass within a sphere of radius 3 kpc from the satellite’s centre: over 12 Gyr in model C the satellite loses about 30% of its stellar mass, while in model E more than 70% of the stellar mass is tidally stripped along the orbit. We note that the reference radius $r = 3 \text{ kpc}$ encloses the large majority of the stellar mass at $t = 0$ (98% in model C and 78% in model E), but is small enough to exclude most of the tidal tails during the orbital evolution.

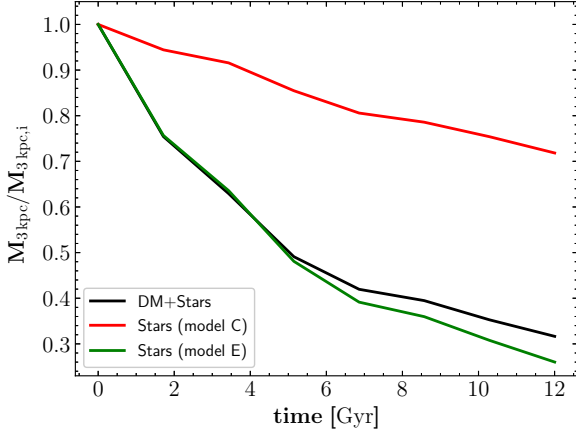


Figure 4. Evolution of the total (DM plus stars) mass (black curve) and of the stellar mass (red curve for model C and green curve for model E) of the satellite in the N -body simulation. Here $M_{3 \text{ kpc}}$ is the mass within 3 kpc from the satellite’s centre and $M_{3 \text{ kpc}, i}$ is the initial value of $M_{3 \text{ kpc}}$.

The extent, density and morphology of the stellar tidal tails can be assessed by looking at Fig. 3, showing, for models C (middle column of panels) and E (right column of panels), the projected stellar density distribution of the satellite at different times in the simulation for a line of sight parallel to the Galactic equatorial plane. The stellar streams are extremely tenuous in model C, while are much more pronounced in model E.

5.2.3 Stellar kinematics

Here we study the stellar kinematics of the satellite and of the streams, focusing in particular on the line-of-sight stellar velocity dispersion σ_{los} . As an illustrative case, we take as line of sight the direction of the y axis in our reference Galactic Cartesian coordinate system and we take as fiducial boundary between the main body of the satellite and the tidal tails $R = 3 \text{ kpc}$, where $R = \sqrt{(x - x_0)^2 + (z - z_0)^2}$ is the projected distance from the satellite’s centre (x_0, z_0) in the xz plane. For the main body of the satellite we compute σ_{los} from sets of particles belonging to circular annuli: the line-of-sight velocity dispersion $\sigma_{\text{los}, j}$ of the j -th radial bin $R_j < R < R_{j+1}$ is given by

$$\sigma_{\text{los}, j}^2 = \frac{\sum_i m_{\star, i} (v_{y, i} - \langle v_y \rangle)^2}{\sum_i m_{\star, i}}, \quad (10)$$

where $v_{y, i}$ is the y component of the velocity of the i -th particle, $\langle v_y \rangle = (\sum_i m_{\star, i} v_{y, i}) / (\sum_i m_{\star, i})$, and the sums are over all particles with $R_j < R_i < R_{j+1}$. Here $m_{\star, i} = \mathcal{P}_{\star}(\mathcal{E}_i) m_i$, where m_i is the mass of the i -th particle and \mathcal{E}_i is its initial energy in the isolated satellite. Fig. 6 shows the satellite’s initial and final profiles of σ_{los} for models C and E. In the initial conditions σ_{los} is higher for model E, which has a flatter stellar density profile, than for model C, which has a steeper stellar density profile (see upper panels of Fig. 5). This just reflects the fact that, for a given gravitational potential, a higher velocity dispersion is needed to maintain in equilibrium a more extended stellar component. For both models the final σ_{los} profile has a shape similar to the corresponding initial profile, but lower normalization: σ_{los} decreases with time mainly because the potential well becomes shallower, owing to substantial mass loss (see Fig. 5, lower panels).

It is also interesting to assess how the kinematics of the stellar tidal tails depends on the initial stellar density distribution. For this purpose we consider the $t = 12 \text{ Gyr}$ snapshot and, taking again the y axis as line of sight, we distinguish the leading tail (lying above and to the right of the satellite in the bottom panels of Fig. 3) and the trailing tail (lying to the left of the satellite in the bottom panels of Fig. 3). Specifically, we assign to the leading tail all particles with $R > 3 \text{ kpc}$ and $z > z_0 - 1.8(x - x_0)$, and to the trailing tail all particles with $R > 3 \text{ kpc}$ and $z < z_0 - 1.8(x - x_0)$, with $x_0 = 31.9 \text{ kpc}$ and $z_0 = -124.8 \text{ kpc}$. σ_{los} as a function of R is shown in Fig. 7 for the leading and trailing tails of models C and E. For given model, the two tails have similar σ_{los} profiles out to $R \approx 40 \text{ kpc}$: at larger distances from the satellite the leading tail tends to have higher stellar velocity dispersion than the trailing tail. For given tail (leading or trailing), the σ_{los} profile is systematically higher for model E than for model C, which reflects the higher velocity dispersion of the stellar component of model E in the initial conditions (Fig. 6). To quantify the overall velocity dispersion of each tail, we compute the quantity $\sigma_{\text{los}, \text{tail}}$, defined by

$$\sigma_{\text{los}, \text{tail}}^2 = \frac{\sum_{j=1}^{N_{\text{bin}}} \sigma_{\text{los}, j}^2 \Sigma_{\star, j}}{\sum_{j=1}^{N_{\text{bin}}} \Sigma_{\star, j}}, \quad (11)$$

where $\sigma_{\text{los}, j}$ and $\Sigma_{\star, j}$ are, respectively, the line-of-sight stellar velocity dispersion and stellar surface density of the j -th radial bin of the tail (we used $N_{\text{bin}} = 24$ bins uniformly spaced in R between $R \approx 3 \text{ kpc}$ and $R \approx 100 \text{ kpc}$). The leading tail has $\sigma_{\text{los}, \text{tail}} \approx 2.8 \text{ km s}^{-1}$ for model C and $\sigma_{\text{los}, \text{tail}} \approx 3.6 \text{ km s}^{-1}$ for model E; the trailing tail has $\sigma_{\text{los}, \text{tail}} \approx 2.8 \text{ km s}^{-1}$ for model C and $\sigma_{\text{los}, \text{tail}} \approx 3.5 \text{ km s}^{-1}$ for model E.

5.2.4 A family of models with smoothly varying \mathcal{P}_{\star}

So far we have applied to our simulation two models (C and E), that is two choices of \mathcal{P}_{\star} . However, the power of the presented method lies in the fact that infinite models can be explored by varying continuously the values of the parameters of \mathcal{P}_{\star} . Thus we illustrate here how some properties of the satellite and of the tails vary in entire family of n models whose extremes are models C and E. The i -th member of this family of models (for $i = 1, \dots, n$) has $\mathcal{P}_{\star}(\mathcal{E})$ given by equation (6) with parameters

$$\alpha = \alpha_C + \frac{i-1}{n-1}(\alpha_E - \alpha_C), \quad (12)$$

$$\beta = \beta_C + \frac{i-1}{n-1}(\beta_E - \beta_C), \quad (13)$$

$$A = A_C + \frac{i-1}{n-1}(A_E - A_C), \quad (14)$$

and

$$\mathcal{E}_0 = \mathcal{E}_{0, C} + \frac{i-1}{n-1}(\mathcal{E}_{0, E} - \mathcal{E}_{0, C}), \quad (15)$$

where $(\alpha_C, \beta_C, A_C, \mathcal{E}_{0, C})$ and $(\alpha_E, \beta_E, A_E, \mathcal{E}_{0, E})$ are the sets of values of parameters of models C and E, respectively (see Section 5.2.2). With this definition we get model C for $i = 1$ and model E for $i = n$; for $1 < i < n$ we get models with $\mathcal{P}_{\star} > 0$ that are intermediate between models C and E: the stellar component is more embedded in the DM halo for lower values of i . Each member of this family of models can be conveniently labelled with the value of its initial ($t = 0$) stellar half mass radius $r_{\text{half}, \star}$ (that is the radius of the sphere

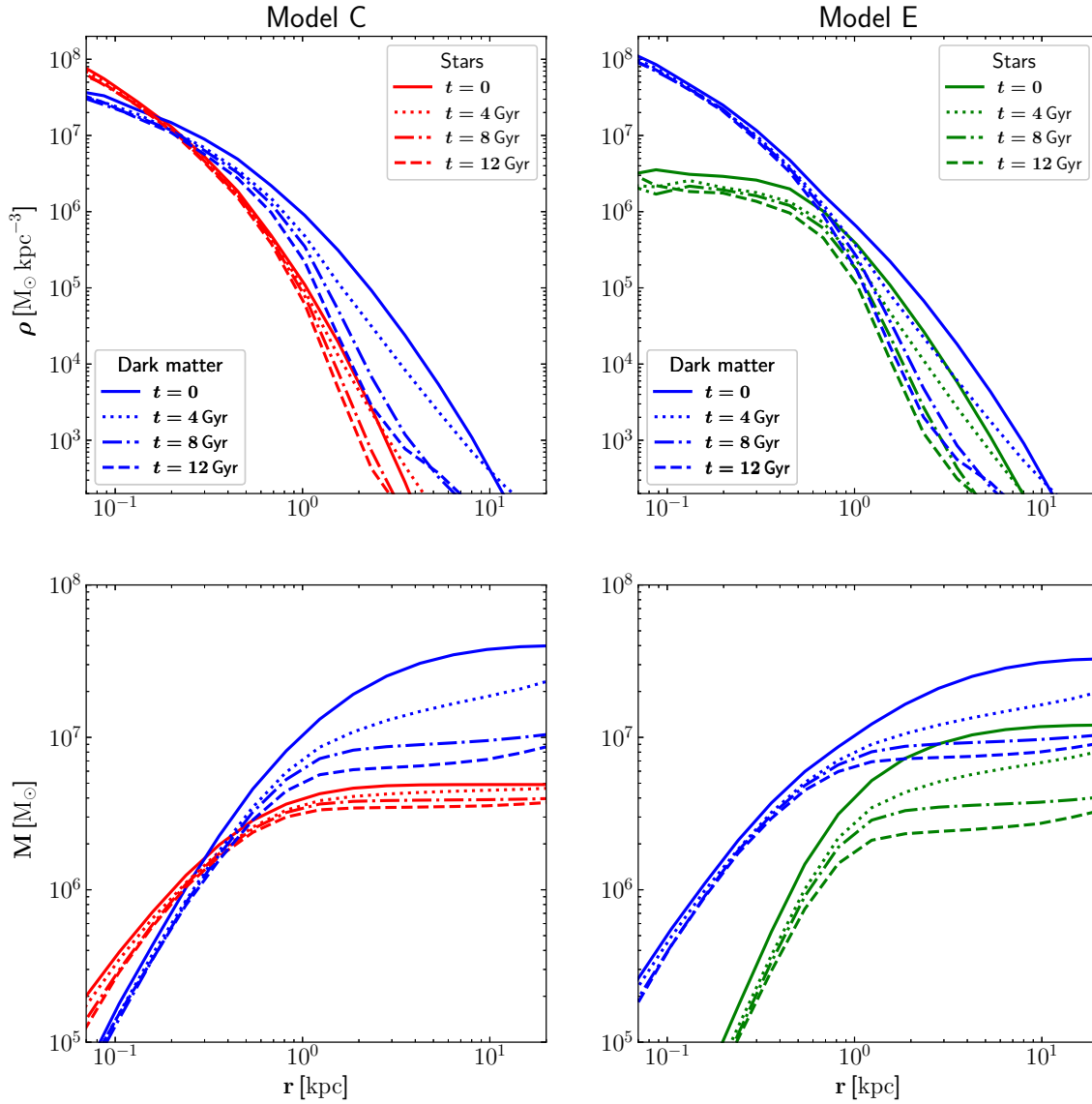


Figure 5. *Upper panels.* Angle-averaged density profiles of the satellite in the N -body simulation at different times, indicated in the legend, for models C (left panels) and E (right panels). The red and green curves represent the stellar density, while the blue curves represent the DM density. *Lower panels.* Stellar and DM mass profiles for the same times and models as in the corresponding upper panels.

containing half of the stellar mass), which increases monotonically with i . The initial stellar density profile of the simulated satellite is shown in Fig. 8 for models C and E, and for three representative intermediate models, labelled with their values of $r_{\text{half},\star}$.

Fig. 9 shows the dependence on $r_{\text{half},\star}$ of some global properties of the stellar component of the simulated satellite for the family of models defined above. The upper panel of Fig. 9 plots the fraction of stellar mass lost (defined as the stellar mass in particles more distant than 3 kpc from the satellite’s centre) as a function of $r_{\text{half},\star}$ after 5 Gyr and 12 Gyr of evolution. The fraction of stellar mass lost

increases smoothly from more embedded (smaller $r_{\text{half},\star}$) to less embedded (larger $r_{\text{half},\star}$) models. The lower panel of Fig. 9 plots the line-of-sight stellar velocity dispersion $\sigma_{\text{los,tail}}$ (see Section 5.2.3) of the leading and trailing tails as a function of $r_{\text{half},\star} \cdot \sigma_{\text{los,tail}}$, which is similar for the two tails for a given model, increases smoothly with $r_{\text{half},\star}$: the less embedded the initial stellar component, the higher the velocity dispersion of the stellar streams.

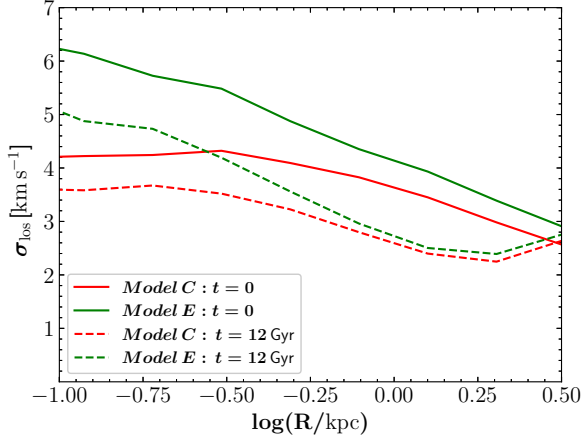


Figure 6. Line-of-sight (along the y axis) stellar velocity dispersion profile for the satellite at the beginning and at the end of the simulation for models C and E.

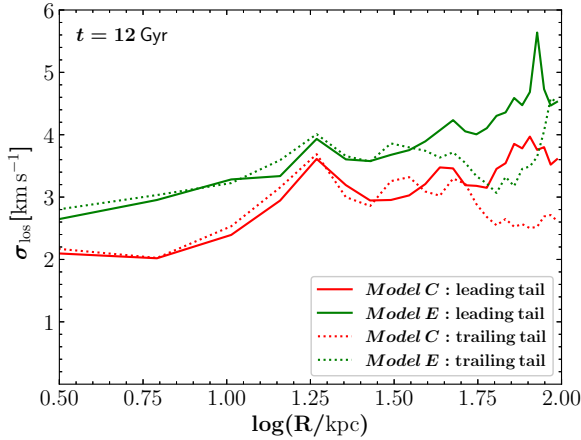


Figure 7. Line-of-sight (along the y axis) stellar velocity dispersion profile of the leading and trailing tidal tails at the end of the simulation for models C and E.

6 DISCUSSION AND CONCLUSIONS

We have presented a new approach to N -body modelling of composite collisionless stellar systems. The method, which we refer to as effective multi-component N -body modelling, allows one to build a one-component system, and interpret it *a posteriori* in infinite ways as a multi-component system using functions of the integrals of motion, dubbed portion functions. In an N -body simulation the construction of the different components can be done in post processing, thus greatly extending the applicability of the simulation. As an example of application, we presented the results of an N -body simulation of a satellite orbiting in the tidal field of the Milky Way, which is interpreted *a posteriori* as a two-component (stars plus DM) system. This example nicely illustrates the potential of the presented method, by showing the dependence of the structure and kinematics of the final satellite and stellar streams on the choice of the portion function.

For simplicity, we have presented as an application only the case in which the parent one-component stellar system is spherical and

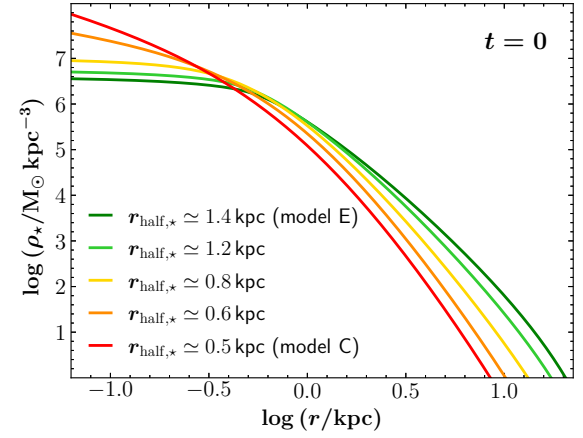


Figure 8. Initial stellar density profile of the simulated satellite for models C and E, and for three intermediate models, labelled with the value of their stellar half-mass radius.

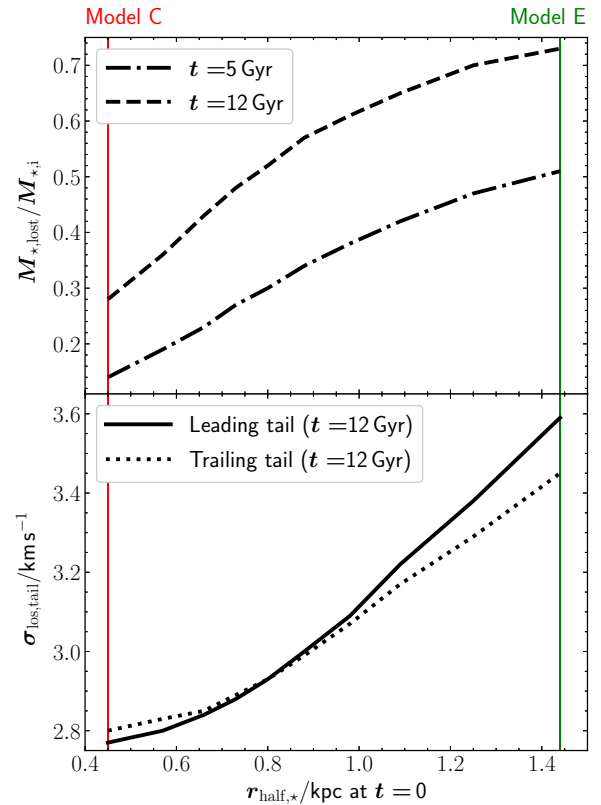


Figure 9. *Upper panel.* Fraction of stellar mass lost by the satellite in the simulation after 5 and 12 Gyr of evolution as a function of the initial stellar half-mass radius for a family of models with smoothly varying initial stellar density distribution, ranging from the compact model C to the extended model E. Here $M_{*,\text{lost}}$ is the stellar mass in particles more distant than 3 kpc from the satellite's centre and $M_{*,i}$ is the initial stellar mass. *Lower panel.* Final line-of-sight stellar velocity dispersion of the leading and trailing tails in the simulation for the same family of models as in the upper panel.

isotropic, and the portion function depends only on the initial particle energy. But the very same method can be applied to anisotropic spherical system as well as to non spherically symmetric systems, provided their DF is known analytically or numerically. For instance, one could build anisotropic multi-component spherical systems with total DF $f_{\text{tot}} = f_{\text{tot}}(\mathcal{E}, L)$, where L is the magnitude of the angular momentum (see [Binney & Tremaine 2008](#)), by using portion functions $\mathcal{P}_k(\mathcal{E}, L)$. A straightforward case is that of Osipkov-Merritt anisotropic spherical models ([Osipkov 1979](#); [Merritt 1985](#)), in which the DF is a function of a single variable Q , which is a combination of \mathcal{E} and L , so $\mathcal{P}_k = \mathcal{P}_k(Q)$. Moreover, the method is not limited to spherical systems, and can be also applied to axisymmetric systems with total DF $f_{\text{tot}} = f_{\text{tot}}(\mathcal{E}, L_z)$, where L_z is the component of the angular momentum along the symmetry axis (see [Binney & Tremaine 2008](#)), using portion functions $\mathcal{P}_k(\mathcal{E}, L_z)$, as well as to both spherical and flattened models with total distribution function $f_{\text{tot}}(\mathbf{J})$ depending on the action integrals \mathbf{J} (e.g. [Binney 2014](#); [Vasiliev 2019](#)), and portion functions $\mathcal{P}_k(\mathbf{J})$.

Of course, the presented effective N -body modelling method has its own limitations. A necessary condition to use the effective modelling, and thus to obtain the components' DFs by subtraction from the total DF, is to know, numerically or analytically, the total DF, which can be straightforward only in systems in which the total distribution is simple, for instance because one of the components (typically the DM halo) is dominant. Moreover, the construction of the portion functions is relatively easy when the shapes of the system's components are simple and similar among each other, but can be unfeasible in very complex configurations. However, as it is well known, the build-up of a complex composite stellar system (for instance an equilibrium galaxy model with disc, bulge and non-dominant dark halo) is a hard task also in standard approaches based on the DFs of the system's components.

The main power of the effective N -body modelling is that the components of a composite simulated stellar system can be assigned in post-processing. This is especially useful when a simulation aims to reproduce an observed distribution of stars, as it is often the case. A typical case is that in which the composite system consists of a stellar component and a DM halo. For a given simulation, one can *a posteriori* explore the space of the free parameters of the stellar portion function (for instance the four-parameter space α, β, A and \mathcal{E}_0 , when \mathcal{P}_* is in the form of equation 6) to find the set of parameters (and thus the initial stellar and DM distributions) such that the final stellar distribution represents best the observed data. In the near future we are going to apply this approach to try to reproduce with N -body simulations the observed properties of satellite dwarf spheroidal galaxies and reconstruct their dynamical evolution and stellar mass loss history.

ACKNOWLEDGEMENTS

FC acknowledges support from grant PRIN MIUR 20173ML3WW00 and from the INAF main-stream (1.05.01.86.31).

DATA AVAILABILITY

The data underlying this article will be shared on reasonable request to the corresponding author.

References

- Battaglia G., Sollima A., Nipoti C., 2015, *MNRAS*, **454**, 2401
 Binney J., 2014, *MNRAS*, **440**, 787
 Binney J., Tremaine S., 2008, *Galactic Dynamics: Second Edition*. Princeton University Press
 Boylan-Kolchin M., Ma C.-P., Quataert E., 2006, *MNRAS*, **369**, 1081
 Ciotti L., Ziaee Lorzad A., 2018, *MNRAS*, **473**, 5476
 Ciotti L., Stiavelli M., Braccisi A., 1995, *MNRAS*, **276**, 961
 Ciotti L., Morganti L., de Zeeuw P. T., 2009, *MNRAS*, **393**, 491
 Ciotti L., Mancino A., Pellegrini S., 2019, *MNRAS*, **490**, 2656
 Dierckx M. I. P., Loeb A., 2017, *ApJ*, **836**, 92
 Eddington A. S., 1916, *MNRAS*, **76**, 572
 Evans N. W., 1993, *MNRAS*, **260**, 191
 Evans N. W., 1994, *MNRAS*, **267**, 333
 Frigo M., Balcells M., 2017, *MNRAS*, **469**, 2184
 Hernquist L., 1990, *ApJ*, **356**, 359
 Hiotelis N., 1994, *A&A*, **291**, 725
 Iorio G., Nipoti C., Battaglia G., Sollima A., 2019, *MNRAS*, **487**, 5692
 Johnston K. V., Spergel D. N., Hernquist L., 1995, *ApJ*, **451**, 598
 Laporte C. F. P., White S. D. M., Naab T., Gao L., 2013, *MNRAS*, **435**, 901
 Laporte C. F. P., Johnston K. V., Gómez F. A., Garavito-Camargo N., Besla G., 2018, *MNRAS*, **481**, 286
 Lokas E. L., Kazantzidis S., Majewski S. R., Law D. R., Mayer L., Frinchaboy P. M., 2010, *ApJ*, **725**, 1516
 Londrillo P., Nipoti C., Ciotti L., 2003, *Memorie della Societa Astronomica Italiana Supplementi*, **1**, 18
 Merritt D., 1985, *AJ*, **90**, 1027
 Nipoti C., Londrillo P., Ciotti L., 2003a, *MNRAS*, **342**, 501
 Nipoti C., Stiavelli M., Ciotti L., Treu T., Rosati P., 2003b, *MNRAS*, **344**, 748
 Nipoti C., Cannarozzo C., Calura F., Sonnenfeld A., Treu T., 2020, *MNRAS*, **499**, 559
 Osipkov L. P., 1979, *Soviet Astronomy Letters*, **5**, 42
 Sanders J. L., Evans N. W., Dehnen W., 2018, *MNRAS*, **478**, 3879
 Schechter P., 1976, *ApJ*, **203**, 297
 Ural U., Wilkinson M. I., Read J. I., Walker M. G., 2015, *Nature Communications*, **6**, 7599
 Vasiliev E., 2019, *MNRAS*, **482**, 1525
 Vasiliev E., Belokurov V., Erkal D., 2020, *arXiv e-prints*, p. [arXiv:2009.10726](https://arxiv.org/abs/2009.10726)
 White S. D. M., 1980, *MNRAS*, **191**, 1P